Pressure-induced local structural crossover in a high-entropy metallic glass

Xin Zhang,[1] Hongbo Lou,[1] Fei Zhang,[2,3] Hengwei Luan,[4] Tao Liang ©,[1,5] Shubin Li,[1] Xiehang Chen,[1] Yang Shao,[4] Ke-Fu Yao,[4,*] Zhidan Zeng,[1] and Qiaoshi Zeng ©[1,†]

[1]*Center for High Pressure Science and Technology Advanced Research, Pudong, Shanghai 201203, People's Republic of China*
[2]*Institute of High Energy Physics, Chinese Academy of Sciences, Beijing 100049, People's Republic of China*
[3]*Spallation Neutron Source Science Center, Dongguan 523803, People's Republic of China*
[4]*School of Materials Science and Engineering, Tsinghua University, Beijing 100084, People's Republic of China*
[5]*Jiangsu Key Laboratory of Advanced Metallic Materials, School of Materials Science and Engineering, Southeast University, Nanjing 211189, People's Republic of China*

Achieving effective tuning of glass structures between distinct states is intriguing for fundamental studies and applications, but has previously turned out to be challenging in practice. High-entropy metallic glasses (HEMGs), as an emerging type of metallic glasses (MGs) based on the high-entropy effect, are expected to have more disordered and frustrated chemical short-range structure compared with conventional MGs. Therefore, HEMGs may offer possibilities for structure and properties tuning in glasses. In this work, we employ pressure as a tuning parameter and monitor the atomic structural evolution of a senary HEMG, $Ti_{16.7}Zr_{16.7}Hf_{16.7}Cu_{16.7}Ni_{16.7}Be_{16.7}$, up to ∼40 GPa using *in situ* synchrotron x-ray diffraction. Analysis of its structure factor in reciprocal space and reduced pair distribution function in real space both reveal a pressure-induced structural crossover at ∼20 GPa with a dramatic change in short-range order (SRO), while no similar phenomenon is observed in a conventional MG, $Cu_{36}Zr_{64}$, as a control sample, suggesting the pressure-induced highly tunable SRO in HEMGs originates from the local chemical complexity, namely, the high-entropy effect. These results confirm that enhanced flexibility and tunability of atomic structures could be achieved by introducing the high-entropy effect into MGs. Therefore, configurational entropy could be another dimension for exploring MGs with highly tunable structures and properties for various potential applications.

I. INTRODUCTION

Metallic glasses (MGs) have been the focus of intense research in the advanced metallic materials community due to their importance for both fundamental studies and practical applications [1–3]. Like conventional crystalline alloys, MGs usually consist of one or two principal elements with some other minor alloying elements, which are randomly arranged both chemically and topologically. Recently, a new concept of alloy design based on entropic contributions to the thermodynamic landscape, rather than from cohesive energy, was proposed [4,5]. This strategy was explored by deliberately incorporating five or more elemental species with equimolar or near-equimolar ratios into a single alloy system. Due to the engineered high configurational entropy, these chemically complex systems can be surprisingly stabilized into single-phase solid solutions with simple crystalline structures. These alloys usually possess high structural stability at extremely high or low temperatures and many desirable properties, distinguishing themselves as a novel type of alloy, high-entropy alloys (HEAs) [6–8]. As an amorphous analogy of HEAs, MGs with similar complex compositions and highly disor-

dered topological structure have also been developed, the so-called high-entropy MGs (HEMGs) [9]. The conventional MGs are recognized to have a short-range order (SRO) of solute-centered cluster structure with the principal element as the solvent [10]. In HEMGs, since there are no easily identifiable solute and solvent elements, a more complex or flexible chemical and topological environment is expected.

In HEAs, high configurational entropy is an important factor in stabilizing their structures by lowering the Gibbs free energy. According to the definition of Gibbs free energy ($G = PV - ST$), it is clear that pressure can also play a critical role as a competing or interacting factor of entropy. Pressure-induced structural transitions are widely reported in various materials [11–17], also including HEAs [18,19]. Given the local chemical complexity (high-entropy effect) combined with the topological disorder (no constraint of crystalline symmetry in HEAs), HEMGs are expected to be more flexible and even highly tunable in their atomic arrangement, especially under high pressure compared to either HEAs or conventional MGs, which is intriguing, and yet to be explored.

In this work, using *in situ* high-pressure synchrotron x-ray diffraction (XRD), the structural evolution of a senary $Ti_{16.7}Zr_{16.7}Hf_{16.7}Cu_{16.7}Ni_{16.7}Be_{16.7}$ HEMG sample is studied up to ∼40 GPa in a symmetric diamond anvil cell (DAC). According to the structure factors $S(q)$ and reduced pair distribution function $G(r)$ data derived from XRD as a function
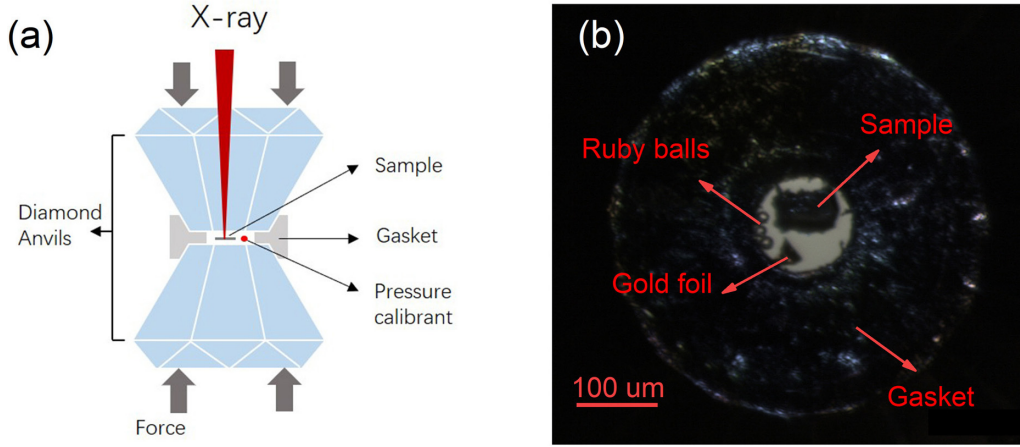
FIG. 1. A schematic illustration of the experimental setup (a) and an optical sample image of the $Ti_{16.7}Zr_{16.7}Hf_{16.7}Cu_{16.7}Ni_{16.7}Be_{16.7}$ HEMG loaded in a DAC (b). The scale bar in (b) represents 100 μm.

of pressure, we find that when the pressure reaches $\sim$20 GPa, changes in SRO of the HEMG reveal apparent atomic rearrangement and even extend into medium-range order (MRO). This phenomenon is suggested to be attributed to the different responses to pressure for the diverse atomic pairs. These results demonstrate that HEMGs could have more structural flexibility for tuning, opening up an avenue toward unexplored space for MG design and development.

II. EXPERIMENTAL DETAILS

A senary $Ti_{16.7}Zr_{16.7}Hf_{16.7}Cu_{16.7}Ni_{16.7}Be_{16.7}$ bulk HEMG [20] with high chemical complexity is chosen as our model system for *in situ* high-pressure synchrotron XRD experiments. Master ingots were prepared by arc melting of pure elements ($>$99.9at. %) under a high-purity argon atmosphere using a Ti ingot as an oxygen getter. The master ingots were flipped and remelted at least four times to ensure chemical homogeneity, followed by casting the melt into a water-cooled copper mold. The resulting cylindrical samples are $\sim$3 mm in diameter. Ingots of a conventional $Cu_{36}Zr_{64}$ MG are also prepared by arc melting. $Cu_{36}Zr_{64}$ ribbons with a thickness of $\sim$20 μm were produced by the melt-spinning method with a single copper roller under a high-purity argon atmosphere. Their amorphous nature was verified by an in-house x-ray diffractometer (Panalytical-Empyrean, Cu $K\alpha$ radiation) and a differential scanning calorimeter (Netzsch, DSC 404 F3).

In situ high-pressure synchrotron XRD experiments with an x-ray wavelength of 0.3220 Å and a focused beam ($\sim$3.5 $\times$ 4 μm^2) by a Kirkpatrick-Baez (KB) mirror system were performed on the $Ti_{16.7}Zr_{16.7}Hf_{16.7}Cu_{16.7}Ni_{16.7}Be_{16.7}$ at the beamline 13-IDD of Advanced Photon Source (APS), Argonne National Laboratory (ANL), USA. The XRD patterns were collected by a Mar165 charge-coupled device (CCD) detector placed at $\sim$190 mm away from samples, and LaB_6 was used as a standard for detector calibration. The samples were all cut into tiny pieces with sizes of approximately 60 $\times$ 40 $\times$ 20 μm^3 and then were loaded into a symmetric DAC with the anvil culet size of $\sim$400 μm. Tiny ruby balls and gold foil were loaded beside the sample as pressure calibrants using the ruby fluorescence pressure scale [21] and

Au equation of state [22], respectively. The gasket was T301 stainless steel, and the sample chamber was a hole with a diameter of $\sim$100 μm drilled by laser in the gasket indent (preindented to $\sim$20 GPa using the same DAC). The 4:1 methanol-ethanol mixture [23,24] was loaded into the DAC as the pressure-transmitting medium. A schematic illustration of the experimental setup and an optical image of the sample loaded in a DAC are shown in Fig. 1. After increasing pressure to a target value, the pressure was carefully stabilized to ensure the pressure fluctuation in the sample chamber before and after each XRD exposure was less than 0.2 GPa. The background patterns were collected at each pressure by shining the x-ray beam on the empty area inside the sample chamber. Two-dimensional (2D) XRD images were integrated to obtain the one-dimensional $I(q)$ patterns using the software DIOPTAS [25] (see Supplemental Material [26] for more information about XRD data correction and process).

The total scattering factor, $S(q)$ ($q = 4\pi \sin\theta/\lambda$, λ is the x-ray wavelength, and 2θ is the angle between the incident and diffraction x-ray beam) [27], and the reduced pair distribution function $G(r)$ can be derived from $I(q)$ using the PDFGETX3 software package [28]. $S(q)$ is obtained from the coherently scattered intensity $I^{coh}(q)$,

$$S(q) = 1 + \frac{I^{coh}(q) - \langle f^2 \rangle}{\langle f \rangle^2}, \tag{1}$$

where $\langle f \rangle = \sum_{i=1}^{n} c_i f_i(q)$ and $\langle f^2 \rangle = \sum_{i=1}^{n} c_i f_{i=1}^2(q)$, in which c_i corresponds to the atomic fraction of the component i with an x-ray atomic scattering factor $f_i(q)$. The $G(r)$ function was derived from the sine-Fourier transform of the $S(q)$ data by the following relation:

$$G(r) = 4\pi r[(\rho(r) - \rho_0] = \frac{2}{\pi}\int_0^\infty q[S(q) - 1]\sin(qr)dq. \tag{2}$$

The pair correlation function $g(r)$ can be calculated from the experimentally determined reduced pair distribution function $G(r)$ by
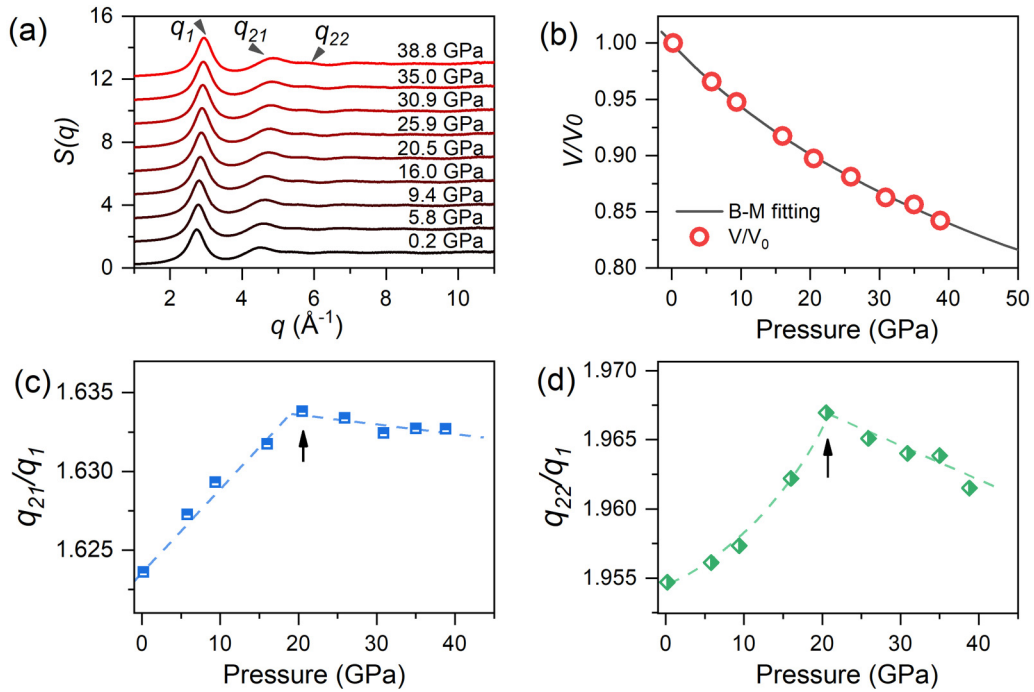
$$g(r) = \frac{G(r)}{4\pi r \rho_0} + 1. \tag{3}$$

FIG. 2. The structure evolution of the $Ti_{16.7}Zr_{16.7}Hf_{16.7}Cu_{16.7}Ni_{16.7}Be_{16.7}$ HEMG in reciprocal space during compressing. (a) Structure factors $S(q)$ during compression from 0.2 to 38.8 GPa. (b) The reduced volume V/V_0 as a function of pressure. The solid gray line is the fit to the third-order BM-EOS with the bulk modulus $B_0 = 148.9 \pm 6.6$ GPa and the pressure derivative $B' = 4.9 \pm 0.6$. The peak position ratios of q_{21}/q_1 (c) and q_{22}/q_1 (d) as a function of pressure consistently show a crossover at $\sim$20 GPa. The gray dashed lines are guides to the eye.

Coordination numbers can be obtained from radial distribution functions, RDF(r),

$$RDF(r) = 4\pi r^2 \rho(r) = 4\pi r^2 \rho_0 + rG(r), \quad (4)$$

where $\rho(r)$ and ρ_0 represent the local and average atomic number density at a given temperature and pressure condition, respectively. The x-ray weighting factors of atomic pairs, w_{ij}, are calculated as

$$w_{ij} = \frac{(2 - \sigma_{ij})c_i c_j f_i(q) f_j(q)}{\sum_{ij} c_i c_j f_i(q) f_j(q)}, \quad \sigma_{ij} = \begin{cases} 1, & i = j \\ 0, & i \neq j. \end{cases} \quad (5)$$

In situ high-pressure synchrotron XRD experiments with an x-ray wavelength of 0.2895 Å and a focused beam size of $7.7 \times 3.3\,\mu m^2$) were performed on the $Cu_{36}Zr_{64}$ MG at the beamline P02.2, PETEA-III, Desy, Germany [29]. 2D XRD patterns were collected using a 2D PerkinElmer amorphous *a*-Si detector. The exposure time for each XRD pattern was set to 10 s and accumulated 10 times for better statistics. The position and orientation of the detector to the x-ray beam were calibrated using the diffraction pattern of a CeO_2 standard. Details of the sample loading and data analysis are the same as those described for the HEMG sample.

III. RESULTS

After background subtraction and corrections of the raw XRD data, the total structure factors $S(q)$ of the HEMG sample with q coverage up to $\sim$11 Å^{-1} from 0.2 to 38.8 GPa are obtained and shown in Fig. 2(a). In the studied pressure range, the HEMG sample keeps its amorphous structure, and the whole $S(q)$ patterns shift to higher q values as expected

for the pressure-induced volume shrinkage. Figure 2(b) shows the relative atomic volume, estimated by an empirical power law relationship previously established for room temperature compression of MGs, $V(P)/V(0) = [q_1(0)/q_1(P)]^{2.5}$, as a function of pressure, where q_1 is the first peak position in $S(q)$ and V is the average atomic volume, where V is the sample volume and q_1 is the peak position of the principal diffraction peak. It should be noted that although the power value may vary slightly depending on a specific composition, choosing different power values does not affect the judgment about phase transitions, which rely on discontinuous changes or kinks in the volume-pressure curve. A monotonic decrease of atomic volume is observed upon increasing pressure. The volume-pressure dependence can be well described by a third-order Birch-Murnaghan (BM) equation of state (BM-EOS) [30], which indicates no apparent first-order (volume collapse) phase transitions occurring during compression. Compared with the structural information reflected by the first peak of $S(q)$, the fluctuations at a higher q range can reveal more local structural information; e.g., the two peak position ratios, q_{21}/q_1 and q_{22}/q_1 (q_{21} and q_{22} are the peak position of the second peak and its shoulder, respectively), are widely studied as characteristics of SRO [31–33]. The evolution of the two ratios as a function of pressure is depicted in Figs. 2(c) and 2(d), respectively. The pressure dependence of the two ratios changes sharply at $\sim$20 GPa, showing an unusual crossover at $\sim$20 GPa. This result suggests a change in SRO of this HEMG at $\sim$20 GPa. In order to get more direct information on SRO in real space, the reduced pair distribution function, $G(r)$, describing the probability of finding an atom at a distance of r from a given atom, is
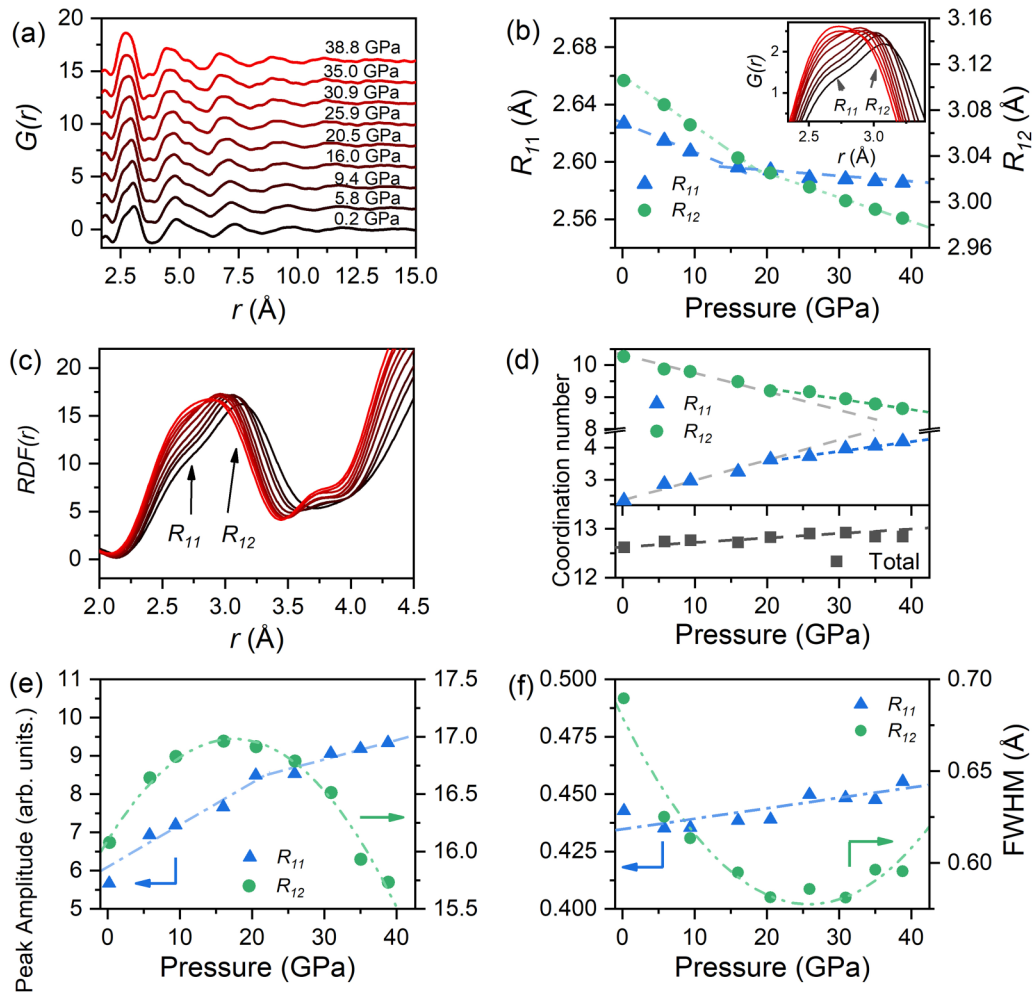
FIG. 3. The structural evolution of the $Ti_{16.7}Zr_{16.7}Hf_{16.7}Cu_{16.7}Ni_{16.7}Be_{16.7}$ HEMG in real space during compressing. (a) Reduced pair distribution function $G(r)$ during compression from 0.2 to 38.8 GPa. (b) The peak positions of two subpeaks are deconvoluted from the first (inset) peak in $G(r)$ as a function of pressure. (c) Radial distribution functions, $RDF(r)$. The peak area (coordination number) (d), amplitude (e), and width (f) of the two subpeaks deconvoluted from the first peak in $RDF(r)$ as a function of pressure. All the dashed lines are guides to the eye.

further derived from the sine-Fourier transform of the $S(q)$. Figure 3(a) shows the $G(r)$ data from 0.2 to 38.8 GPa. The profile of the first nearest-neighbor shell in $G(r)$ presents the most prominent structural variations rather than pure elastic shrinkage upon increasing pressure. In the inset of Fig. 3(b), the first nearest-neighbor shell shows a stratified structure with two major subpeaks, and the right subpeak R_{11} has a lower amplitude than the left subpeak R_{12} at low pressures. During compression, besides the left shift of the first shell, the relative amplitude of the two different subpeaks also varies significantly. To derive more quantitative information on the changes in SRO, the first shell in $G(r)$ is fitted by two Gaussian peaks. In Fig. 3(b), the peak positions of the two subpeaks, R_{11} and R_{12}, consistently show abrupt changes when compressed to ∼20 GPa. The radial distribution functions, $RDF(r)$, are further calculated and shown in Fig. 3(c). The coordination numbers of the two subpeaks as a function of pressure are estimated and shown in Fig. 3(d). The coordination number of the subpeak R_{11} slightly increases with pressure while it decreases for the subpeak R_{12}. In addition, the slope of the coordination number versus pressure of both subpeaks

also decreases at ∼20 GPa. However, the total coordination number of the entire first shell slightly and monotonically increases with pressure [Fig. 3(d)]. Moreover, the changes of other fitting parameters, amplitude and full width at half maximum (FWHM), of the first peak of $RDF(r)$ are presented in Figs. 3(e) and 3(f), respectively, which both present distinct compression behavior. The subpeak, R_{12}, in particular, shows a crossover at ∼20 GPa in both the amplitude and the FWHM. Although without a periodic symmetry, structural changes of SRO in glasses will naturally and inevitably extend into longer length scales, e.g., through the well-recognized linkages between SRO clusters and MRO. Looking at the structural information at an extended length scale in $G(r)$, the splitting of the second peak is quite common, which carries information on different connection methods between clusters forming MRO in MGs [34–37]. According to the hard-sphere model, four connection methods can be identified according to the subpeak positions ratio of the second peak of $G(r)$ with respect to the average cluster radius, r_1, e.g., $2r_1$, $\sqrt{3}r_1$, $\sqrt{8/3}r_1$, and $\sqrt{2}r_1$, correspond to one-atom (vertex) sharing, two-atom (edge) sharing, three-atom (face) sharing, and
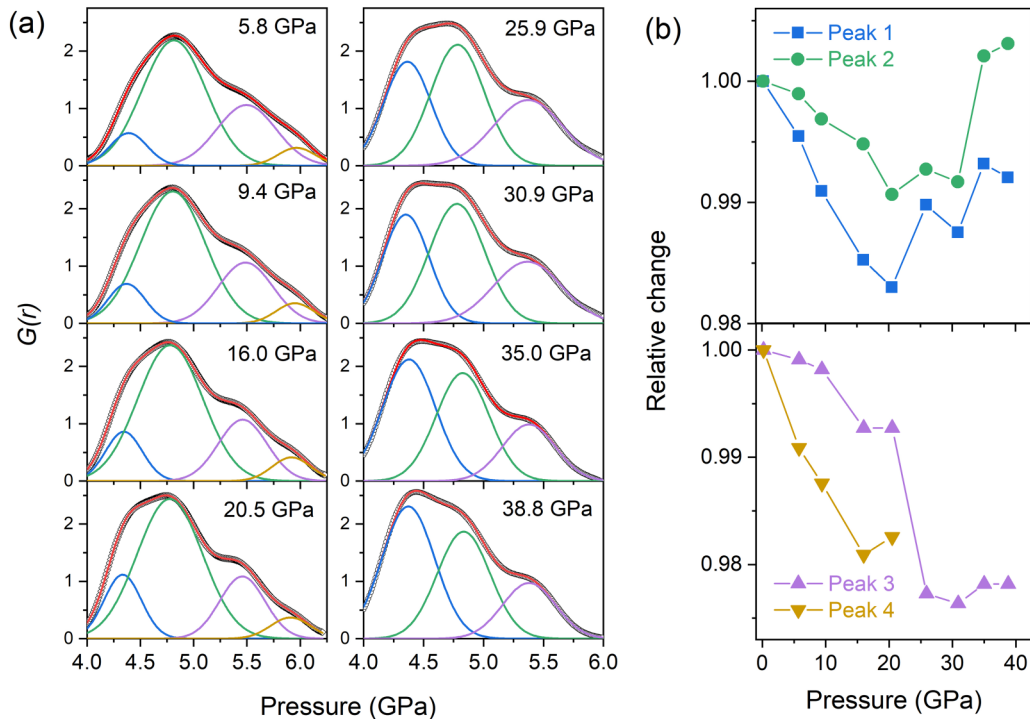
FIG. 4. The MRO evolution of the $Ti_{16.7}Zr_{16.7}Hf_{16.7}Cu_{16.7}Ni_{16.7}Be_{16.7}$ HEMG in real space during compressing. (a) Deconvolution of the second peak of $G(r)$ into several Gaussian subpeaks at representative pressures. (b) The evolution of reduced peak position of the subpeaks as a function of pressure.

four-atom (face) sharing [34–37], respectively. For further analysis, the second peak of $G(r)$ at different pressures is fitted by several Gaussian peaks with a linear background [Fig. 4(a)], and the normalized peak positions of these fitted Gaussian peaks are shown in Fig. 4(b). At relatively low pressures, four Gaussian peaks are required to fit the curve, while above 20 GPa, only three peaks are needed to obtain the same fitting quality ($R^2 \geqslant 0.999$), indicating that the linkage modes between clusters may have changed significantly at ∼20 GPa. Specifically, above 20 GPa, the intensity of the first subpeak (four-atom sharing) increases sharply and begins to be dominant (denser packing in MRO), while the other relatively loose connection modes begin to weaken or even disappear (one-atom sharing). For peak positions [Fig. 4(b)], different from the simple left shift under low pressure, above ∼20 GPa, the first and second peaks move to the right with increasing pressure, while the peak position of the third peak shows a sudden contraction. This distinct behavior of subpeak positions of $G(r)$ also further supports the crossover of connection modes in MRO at ∼20 GPa accompanying the changes in SRO.

It is noted that the discussion above is based on the hard-sphere model, so the above analysis is more rational to explain the splitting of the second peak in $G(r)$ in a single elemental system [34]. For multicomponent systems such as HEMGs, quantitative analysis based on an accurate structural model is challenging due to the complexity of topological and chemical structures in SRO. However, in this work, structural changes are pretty pronounced (the disappearance of the fourth fitting peak and the abrupt changes of the peak position and intensity of the subpeaks); thus, a crossover in the structural

connectivity modes in MRO of the HEMG still can be unambiguously identified.

Moreover, in order to further clarify the origin of the structural evolution of the HEMG under high pressure, a conventional binary MG, $Cu_{36}Zr_{64}$, was also studied during compressing up to 30 GPa with similar experimental conditions. However, in both reciprocal and real spaces, the $Cu_{36}Zr_{64}$ MG only exhibits monotonous pressure-induced structural shrinkage, and there is no obvious structural rearrangement (Fig. 5).

IV. DISCUSSION

Pressure-induced structural transition in MGs is not rare and has been observed in some rare earth based MGs and other MGs with tunable electronic structures. For these systems, when the applied pressure is high enough, pressure-induced electronic transitions occur, such as delocalization of $4f$ electrons in Ce-based MGs [38] or charge transfer between different species in Ca-Al [39] or Pd-Ni-P [40] MGs. Electronic transitions will usually cause a collapse of atomic volume or changes in local atomic bonding, resulting in dramatic changes in density and atomic rearrangement of the entire system. The most intuitive manifestation of these phenomena is usually a change in EOS with a volume collapse [38] or deviation [39,40]. On the other hand, in a conventional MG system without any electronic or bonding change, the entire compression process could be a fully elastic shrinkage of the initial structure, in which the $S(q)$ and $G(r)$ patterns at high pressures highly resemble those at low pressures in profile [41,42]. However, detailed structural
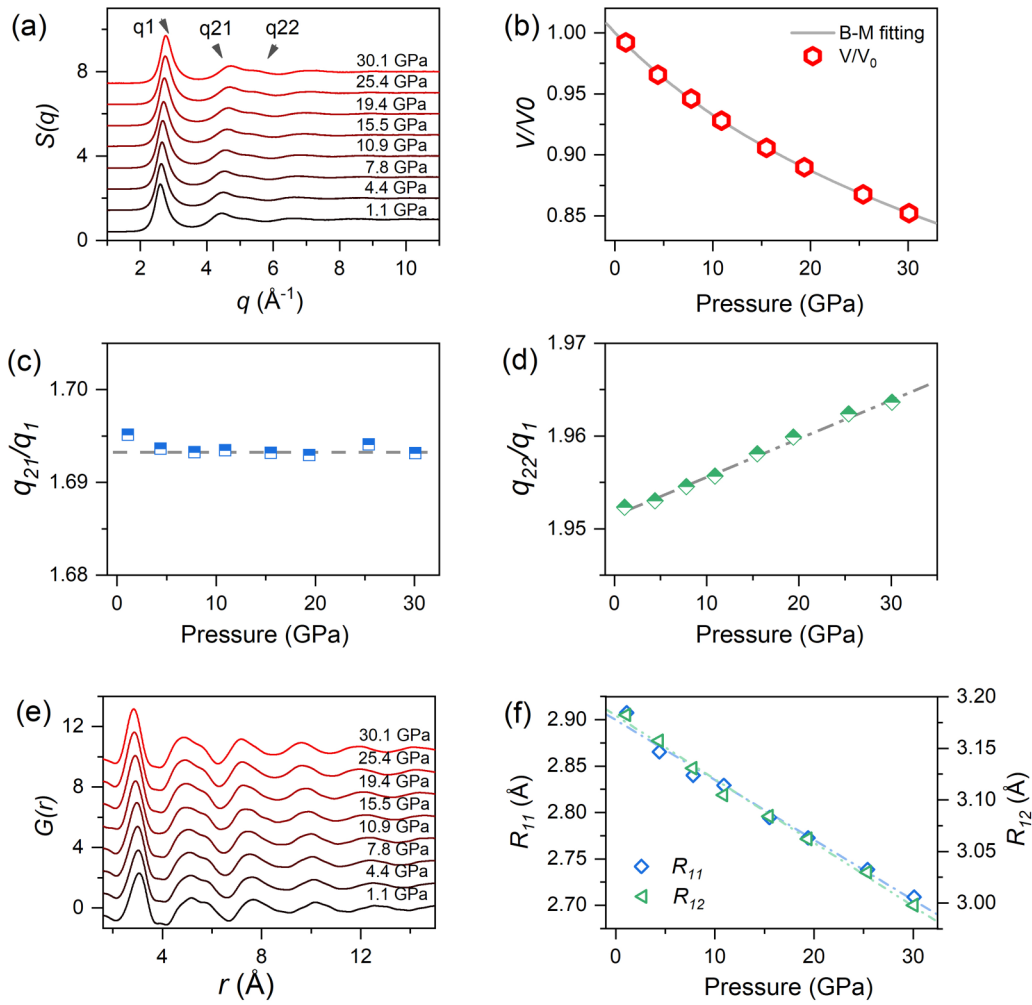
FIG. 5. The structure evolution of the $Cu_{36}Zr_{64}$ MG during compressing. (a) Structure factors, $S(q)$, during compression from 1.1 to 30 GPa. (b) The reduced volume V/V_0 calculated by the power law, $V(P)/V(0) = [q_1(0)/q_1(P)]^{2.5}$, as a function of pressure. The solid gray line is the fit to the third-order BM-EOS with the bulk modulus $B_0 = 117.1 \pm 1.1$ GPa and the pressure derivative $B' = 6.0 \pm 0.2$. The peak position ratios of q_{21}/q_1 (c) and q_{22}/q_1 (d) as a function of pressure show no crossover as observed in the HEMG. (e) The reduced pair distribution function $G(r)$ during compression from 1.1 to 30 GPa. (f) The peak positions of the two subpeaks deconvoluted from the first peak in $G(r)$ of the $Cu_{36}Zr_{64}$ MG as a function of pressure, which show a perfect linear relationship without any sign of a structural crossover. The gray dashed lines are guides to the eye.

information obtained by quantitative analysis of the peaks in $S(q)$ and $G(r)$ focusing on SRO (inevitably extends into MRO) reveals a structural crossover occurring at ~20 GPa in the $Ti_{16.7}Zr_{16.7}Hf_{16.7}Cu_{16.7}Ni_{16.7}Be_{16.7}$ HEMG system without any element prone to having electronic transitions under pressure. For the 4:1 methanol-ethanol mixture, considerable shear stress will show up and develop above its hydrostaticity limit (~10 GPa) [23,24], which may play a non-negligible role in phase transitions [43]. In our experiments, no dramatic changes were observed in both MGs at ~10 GPa coinciding with the hydrostaticity limit of the pressure medium. Moreover, with the same pressure medium, no structural crossover is observed in the conventional binary $Cu_{36}Zr_{64}$ MG. These results suggest that the structural crossover observed in the HEMG should be associated with the sample itself rather than the nonhydrostaticity that emerged in the pressure medium.

For a multicomponent alloy system, this structural crossover is most likely attributed to a local structural rearrangement due to diverse responses to pressure of the multiple components at high enough pressures, which, however, smears out when we look at the averaged structure over all components. Therefore, the mechanism for the structural crossover reflected by changes in SRO should lie in the details of how each atomic pair responds to compression. However, there are 21 different atomic pairs in the senary $Ti_{16.7}Zr_{16.7}Hf_{16.7}Cu_{16.7}Ni_{16.7}Be_{16.7}$ HEMG, so it is technically challenging to distinguish each atomic pair in this alloy. Since there is no electronic transition reported for these elements in the studied pressure range, we speculate that the atomic rearrangement may result from mutually incompatible compressibility among the 21 diverse atomic pairs. This speculation can be qualitatively confirmed by comparison between the profile of the first peak of $G(r)$ and the distribution of the 21 atomic pairs in distances and their x-ray scattering weights [Fig. 6(a)]. Assuming random pairing is based on the hard-sphere model and the change of bond length
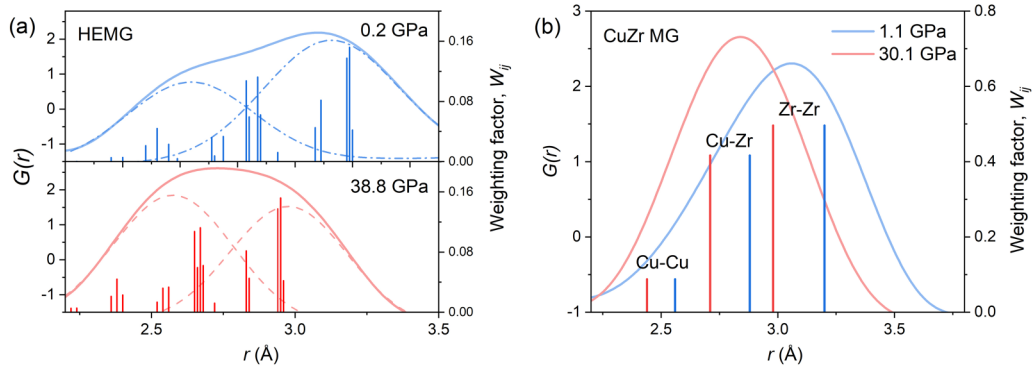
FIG. 6. Comparison of the evolution of atomic pair distribution during compression in the first atomic shell. The distances and x-ray scattering weights of atomic pairs (vertical lines) in the first peak of $G(r)$ at two different pressures for the $Ti_{16.7}Zr_{16.7}Hf_{16.7}Cu_{16.7}Ni_{16.7}Be_{16.7}$ HEMG (a) and the $Cu_{36}Zr_{64}$ MG (b).

under compression is the same as in pure elements (values are listed in Table I), the atomic pairs will have quite different distributions between 0.2 and 38.8 GPa. The disproportional compression of the 21 atomic pairs can reasonably account for the dramatic change of the first peak profile in $G(r)$. This result suggests that the structural crossover of SRO under high pressure could be attributed to differences in the volume shrinkage for these atoms, namely, the failure of synergy in SRO under compression.

Compared with conventional MGs, the failure of a synergy of SRO clusters (atomic pairs) in compression could be much more severe in HEMGs because of their wider distribution of configurations and more severe local atomic stress [44]. The

TABLE I. The details of the 21 possible atomic pairs in the $Ti_{16.7}Zr_{16.7}Hf_{16.7}Cu_{16.7}Ni_{16.7}Be_{16.7}$ HEMG. The interatomic distances (R_{ij}) are from the database of Young *et al.* [54]. w_{ij} is the x-ray scattering weight.

Atomic pairs ($i-j$)	R_{ij} (Å) (0 GPa)	R_{ij} (Å) (39 GPa)	w_{ij}
Zr-Zr	3.20	2.96	0.04196
Zr-Hf	3.19	2.95	0.15189
Hf-Hf	3.18	2.94	0.13746
Ti-Hf	3.09	2.83	0.08152
Zr-Ti	3.07	2.84	0.04504
Ti-Ti	2.94	2.72	0.01209
Cu-Zr	2.88	2.68	0.06205
Cu-Hf	2.87	2.67	0.11231
Ni-Zr	2.84	2.66	0.05934
Ni-Hf	2.83	2.65	0.10741
Cu-Ti	2.75	2.56	0.03331
Be-Zr	2.72	2.52	0.00743
Be-Hf	2.71	2.52	0.01345
Ni-Ti	2.71	2.54	0.03186
Be-Ti	2.59	2.40	0.00399
Cu-Cu	2.56	2.40	0.02295
Ni-Cu	2.52	2.38	0.04389
Ni-Ni	2.48	2.36	0.02098
Be-Cu	2.40	2.24	0.0055
Be-Ni	2.36	2.22	0.00526
Be-Be	2.24	2.08	0.00033

same analysis shows that $Cu_{36}Zr_{64}$ MG does not have a similar structural crossover at high pressures (Fig. 6(b); atomic pair values are listed in Supplemental Material [26]), which is consistent with results observed before in other conventional binary or quaternary MGs [41,42] and can be explained by the quite compatible compressibility between the atomic pairs. In contrast, for HEMGs, severe local stress inside the initial SRO clusters may quickly develop with increasing pressure due to the mutually incompatible compressibility of diverse atomic pairs. Eventually, at high enough pressures, the initial configuration of SRO may destabilize, and atomic rearrangement inside SRO may take place to lower the elastic energy of the system, but in a gradual way, which differs from a sudden polyamorphic transition in some MGs [38–40] and, therefore, is defined as a structural crossover. This structural crossover is found to be basically reversible during decompression (see Supplemental Material [26] for the comparison of structures before compression and after decompression).

From a thermodynamic point of view, the structural crossover might be driven by the Gibbs free energy. Since the sample volume shows no abnormal behavior but a smooth shrinkage [Fig. 2(b)], the configurational entropy is speculated to play an important role during compression. For a real solution, the total configurational entropy of mixing is the sum of the configurational entropy of mixing for an ideal solution, S_C, and the excess configurational entropy of mixing, S_E. In this work, no composition changes in this HEMG, so S_C can be reasonably assumed to be constant at 14.9 J/mol K throughout the entire process. In contrast, the excess entropy S_E is closely related to the atomic structure details (a function of atomic packing and atomic sizes), which is a key factor affecting the formation and stability of MGs [45,46]. Generally, the larger the difference in the atomic sizes and the higher the atomic packing density, the lower the value of S_E will be [47,48]. Although high pressure should prefer higher packing density, atomic size difference does not necessarily increase accordingly, which mainly depends on the relative compressibility of each atom [49]. For the senary HEMG in this work, the atomic size difference (or atomic size polydispersity, δ) decreases monotonically with pressure (see Supplemental Material [26] for the atomic volume of each component and the atomic size
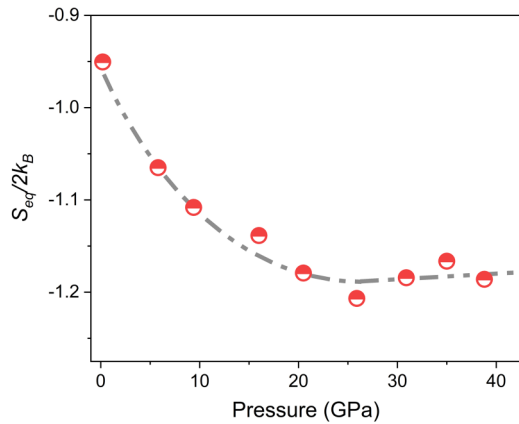
FIG. 7. Equivalent configurational entropy as a function of pressure up to 40 GPa in the $Ti_{16.7}Zr_{16.7}Hf_{16.7}Cu_{16.7}Ni_{16.7}Be_{16.7}$ HEMG. Each point is calculated using Eq. (5) based on $G(r)$ shown in Fig. 2. The dashed line is the guide to the eye.

polydispersity (δ) as a function of pressure). Therefore, S_E may not change monotonously with pressure by considering contributions from both atomic packing density and atomic size polydispersity. In order to quantitatively analyze the evolution of the S_E, the method of Spieckermann *et al.* [50] is adopted, and the "equivalent entropy S_{eq}" is used to replace S_E. The equivalent entropy S_{eq} can be calculated with the equation derived by Nettleton and Green [51,52],

$$S_{eq} = -2\pi \rho_0 k_B \int (g(r) \ln g(r) - g(r) + 1) r^2 dr, \quad (6)$$

where k_B is the Boltzmann constant, ρ_0 is the atom number density, and $g(r)$ is the pair distribution function. The evolution of S_{eq} as a function of pressure is shown in Fig. 7. Below ~ 20 GPa, the value of S_{eq} decreases with increasing pressure, but it turns to increase slightly with pressure above ~ 20 GPa. Obviously, from Eq. (5), it is clear that the value of S_{eq} depends on both the atomic packing density and the local atomic structure (SRO and MRO). Since MGs are typically quite densely packed even at ambient pressure with the maximum coordination number (12–14) of random nearest neighbors [53], the packing density may only slightly increase during compression. Therefore, the pressure-sensitive S_E could dominate the stability of HEMGs and lead to structural modification or crossover.

V. CONCLUSION

In this work, we studied the structural evolution of the $Ti_{16.7}Zr_{16.7}Hf_{16.7}Cu_{16.7}Ni_{16.7}Be_{16.7}$ HEMG during compression up to ~ 40 GPa using *in situ* high-pressure synchrotron XRD. Although no constituent element has pressure-induced electronic transitions in the studied pressure range, a structural crossover in SRO at ~ 20 GPa is explicitly identified by $S(q)$ and $G(r)$. The underlying mechanism for the structural crossover is attributed to the disproportional decrease of various atomic pair distances during compression, which is especially severe in the multicomponent HEMG system with an equal equimolar ratio. From the thermodynamic point of view, this structural feature of HEMG can be characterized by the variable of the excess entropy S_E, which closely correlates with the atomic size misfit and atomic packing; therefore, it is highly pressure sensitive. Using the same experimental technique and data analysis, no similar structural crossover is observed in the conventional MG, $Cu_{36}Zr_{64}$. Given the complex chemical and local topological structures introduced by the diverse multiple principal components in HEMGs, pressure-induced structural tuning or crossover may be general in HEMGs, which could provide good candidate materials for energy absorption applications at extreme conditions requiring no sudden volume changes.

[1] W.-H. Wang, C. Dong, and C. H. Shek, Bulk metallic glasses, Mater. Sci. Eng., R **44**, 45 (2004).

[2] W. L. Johnson, Bulk glass-forming metallic alloys: Science and technology, MRS Bull. **24**, 42 (1999).

[3] Y. Q. Cheng and E. Ma, Atomic-level structure and structure–property relationship in metallic glasses, Prog. Mater. Sci. **56**, 379 (2011).

[4] B. Cantor, I. T. H. Chang, P. Knight, and A. J. B. Vincent, Microstructural development in equiatomic multicomponent alloys, Mater. Sci. Eng. A **375**, 213 (2004).

[5] J. W. Yeh, S. K. Chen, S. J. Lin, J. Y. Gan, T. S. Chin, T. T. Shun, C. H. Tsau, and S. Y. Chang, Nanostructured high-entropy alloys with multiple principal elements: Novel alloy design concepts and outcomes, Adv. Eng. Mater. **6**, 299 (2004).

[6] S. Singh, N. Wanderka, B. S. Murty, U. Glatzel, and J. Banhart, Decomposition in multi-component AlCoCrCuFeNi high-entropy alloy, Acta Mater. **59**, 182 (2011).

[7] Y. Zhang, X. Yang, and P. K. Liaw, Alloy design and properties optimization of high-entropy alloys, JOM **64**, 830 (2012).

[8] Y. Zhang, T. T. Zuo, Z. Tang, M. C. Gao, K. A. Dahmen, P. K. Liaw, and Z. P. Lu, Microstructures and properties of high-entropy alloys, Prog. Mater. Sci. **61**, 1 (2014).

[9] W. H. Wang, High-entropy metallic glasses, JOM **66**, 2067 (2014).

[10] C. J. Byrne and M. Eldrup, Bulk metallic glasses, Science **321**, 502 (2008).

[11] B. Cheng, H. Lou, A. Sarkar, Z. Zeng, F. Zhang, X. Chen, L. Tan, V. Prakapenka, E. Greenberg, and J. Wen, Pressure-induced tuning of lattice distortion in a high-entropy oxide, Commun. Chem. **2**, 1 (2019).

[12] H.-K. Mao, B. Chen, J. Chen, K. Li, J.-F. Lin, W. Yang, and H. Zheng, Recent advances in high-pressure science and technology, Matter Radiat. Extremes **1**, 59 (2016).

[13] Q. Zeng, H. Sheng, Y. Ding, L. Wang, W. Yang, J.-Z. Jiang, W. L. Mao, and H.-K. Mao, Long-range topological order in metallic glass, Science **332**, 1404 (2011).

[14] D. Errandonea, S. G. MacLeod, L. Burakovsky, D. Santamaria-Perez, J. E. Proctor, H. Cynn, and M. Mezouar, Melting curve and phase diagram of vanadium under high-pressure and high-temperature conditions, Phys. Rev. B **100**, 094111 (2019).

[15] H. Saqib, S. Rahman, D. Errandonea, R. A. Susilo, A. Jorge-Montero, P. Rodríguez-Hernández, A. Munoz, Y. Sun, Z. Chen, and N. Dai, Giant conductivity enhancement: Pressure-induced semiconductor-metal phase transition in $Cd_{0.90}Zn_{0.1}Te$, Phys. Rev. B **99**, 094109 (2019).

[16] T. Marqueño, D. Errandonea, J. Pellicer-Porres, D. Santamaria-Perez, D. Martinez-Garcia, E. Bandiello, P. Rodriguez-Hernandez, A. Muñoz, S. N. Achary, and C. Popescu, Polymorphism of praseodymium orthovanadate under high pressure, Phys. Rev. B **103**, 134113 (2021).

[17] A. Liang, R. Turnbull, C. Popescu, F. J. Manjón, E. Bandiello, P. Rodriguez-Hernandez, A. Muñoz, I. Yousef, Z. Hebboul, and D. Errandonea, Pressure-induced phase transition and increase of oxygen-iodine coordination in magnesium iodate, Phys. Rev. B **105**, 054105 (2022).

[18] C. L. Tracy, S. Park, D. R. Rittman, S. J. Zinkle, H. Bei, M. Lang, R. C. Ewing, and W. L. Mao, High pressure synthesis of a hexagonal close-packed phase of the high-entropy alloy CrMnFeCoNi, Nat. Commun. **8**, 1 (2017).

[19] F. Zhang, Y. Wu, H. Lou, Z. Zeng, V. B. Prakapenka, E. Greenberg, Y. Ren, J. Yan, J. S. Okasinski, and X. Liu, Polymorphism in a high-entropy alloy, Nat. Commun. **8**, 15687 (2017).

[20] H. Y. Ding, Y. Shao, P. Gong, J. F. Li, and K. F. Yao, A senary TiZrHfCuNiBe high entropy bulk metallic glass with large glass-forming ability, Mater. Lett. **125**, 151 (2014).

[21] H. K. Mao, J. Xu, and P. M. Bell, Calibration of the ruby pressure gauge to 800 kbar under quasi-hydrostatic conditions, J. Geophys. Res.: Solid Earth **91**, 4673 (1986).

[22] O. L. Anderson, D. G. Isaak, and S. Yamamoto, Anharmonicity and the equation of state for gold, J. Appl. Phys. **65**, 1534 (1989).

[23] X. Chen, H. Lou, Z. Zeng, B. Cheng, X. Zhang, Y. Liu, D. Xu, K. Yang, and Q. Zeng, Structural transitions of 4:1 methanol–ethanol mixture and silicone oil under high pressure, Matter Radiat. Extremes **6**, 038402 (2021).

[24] S. Klotz, J. C. Chervin, P. Munsch, and G. Le Marchand, Hydrostatic limits of 11 pressure transmitting media, J. Phys. D **42**, 075413 (2009).

[25] C. Prescher and V. B. Prakapenka, DIOPTAS: A program for reduction of two-dimensional x-ray diffraction data and data exploration, High Press. Res. **35**, 223 (2015).

[26] See Supplemental Material at http://link.aps.org/supplemental/10.1103/PhysRevB.105.224201 for more information about XRD data correction and process, the list of atomic pairs values in the $Cu_{36}Zr_{64}$ alloy, the comparison of $S(q)$ and $G(r)$ data between the as-prepared and high-pressure recovered HEMG samples, and the atomic volume of each component and the atomic size polydispersity as a function of pressure in the HEMG.

[27] T. Egami and S. J. L. Billinge, *Underneath the Bragg Peaks: Structural Analysis of Complex Materials* (Elsevier, Amsterdam, 2003).

[28] P. Juhás, T. Davis, C. L. Farrow, and S. J. L. Billinge, PDFGETX3: A rapid and highly automatable program for processing powder diffraction data into total scattering pair distribution functions, J. Appl. Crystallogr. **46**, 560 (2013).

[29] H.-P. Liermann, Z. Konopkova, W. Morgenroth, K. Glazyrin, J. Bednarcik, E. E. McBride, S. Petitgirard, J. T. Delitz, M. Wendt, Y. Bican *et al.*, The extreme conditions beamline P02.2 and the extreme conditions science infrastructure at PETRA III, J. Synchrotron Radiat. **22**, 908 (2015).

[30] F. Birch, Finite elastic strain of cubic crystals, Phys. Rev. **71**, 809 (1947).

[31] T. Schenk, D. Holland-Moritz, V. Simonet, R. Bellissent, and D. M. Herlach, Icosahedral Short-Range Order in Deeply Undercooled Metallic Melts, Phys. Rev. Lett. **89**, 075507 (2002).

[32] H. W. Sheng, E. Ma, H. Z. Liu, and J. Wen, Pressure tunes atomic packing in metallic glass, Appl. Phys. Lett. **88**, 171906 (2006).

[33] O. Gross, N. Neuber, A. Kuball, B. Bochtler, S. Hechler, M. Frey, and R. Busch, Signatures of structural differences in Pt–P-and Pd–P-based bulk glass-forming liquids, Commun. Phys. **2**, 1 (2019).

[34] S. P. Pan, J. Y. Qin, W. M. Wang, and T. K. Gu, Origin of splitting of the second peak in the pair-distribution function for metallic glasses, Phys. Rev. B **84**, 092201 (2011).

[35] J. Ding and E. Ma, Computational modeling sheds light on structural evolution in metallic glasses and supercooled liquids, npj Comput. Mater. **3**, 1 (2017).

[36] J. Du and B. Wen, Composition-structure-property correlations of complex metallic alloys described by the "cluster-plus-glue-atom" model, Appl. Mater. Today **7**, 13 (2017).

[37] S. Liu, L. Wang, J. Ge, Z. Wu, Y. Ke, Q. Li, B. Sun, T. Feng, Y. Wu, and J. T. Wang, Deformation-enhanced hierarchical multiscale structure heterogeneity in a Pd-Si bulk metallic glass, Acta Mater. **200**, 42 (2020).

[38] Q.-s. Zeng, Y. Ding, W. L. Mao, W. Yang, S. V. Sinogeikin, J. Shu, H.-k. Mao, and J. Z. Jiang, Origin of Pressure-Induced Polyamorphism in $Ce_{75}Al_{25}$ Metallic Glass, Phys. Rev. Lett. **104**, 105702 (2010).

[39] H. B. Lou, Y. K. Fang, Q. S. Zeng, Y. H. Lu, X. D. Wang, Q. P. Cao, K. Yang, X. H. Yu, L. Zheng, and Y. D. Zhao, Pressure-induced amorphous-to-amorphous configuration change in Ca-Al metallic glasses, Sci. Rep. **2**, 1 (2012).

[40] Q. Du, X.-J. Liu, Q. Zeng, H. Fan, H. Wang, Y. Wu, S.-W. Chen, and Z.-P. Lu, Polyamorphic transition in a transition metal based metallic glass under high pressure, Phys. Rev. B **99**, 014208 (2019).

[41] N. Mattern, J. Bednarcik, H.-P. Liermann, and J. Eckert, Structural behaviour of $Pd_{40}Cu_{30}Ni_{10}P_{20}$ metallic glass under high pressure, Intermetallics **38**, 9 (2013).

[42] H. B. Lou, L. H. Xiong, A. S. Ahmad, A. G. Li, K. Yang, K. Glazyrin, H. P. Liermann, H. Franz, X. D. Wang, Q. P. Cao *et al.*, Atomic structure of $Pd_{81}Si_{19}$ glassy alloy under high pressure, Acta Mater. **81**, 420 (2014).

[43] D. Errandonea, Y. Meng, M. Somayazulu, and D. Häusermann, Pressure-induced $\alpha \rightarrow \omega$ transition in titanium metal: A systematic study of the effects of uniaxial stress, Phys. B: Condens. Matter. **355**, 116 (2005).

[44] S. Luo, J. C. Khong, D. Daisenberger, S. Huang, P. F. McMillan, and J. Mi, Synchrotron x-ray total scattering and modeling study of high-pressure-induced inhomogeneous atom reconfiguration in an equiatomic $Zr_{50}Cu_{50}$ metallic glassy alloy, Phys. Rev. B **105**, 064203 (2022).

[45] G. A. Mansoori, N. F. Carnahan, K. E. Starling, and T. W. Leland Jr., Equilibrium thermodynamic properties of the mixture of hard spheres, J. Chem. Phys. **54**, 1523 (1971).

[46] Y. F. Ye, Q. Wang, J. Lu, C. T. Liu, and Y. Yang, The generalized thermodynamic rule for phase selection in multicomponent alloys, Intermetallics **59**, 75 (2015).

[47] Y. S. Yun, H. S. Nam, P. R. Cha, W. T. Kim, and D. H. Kim, Effects of atomic size difference and heat of mixing parameters on the local structure of a model metallic glass system, Met. Mater. Int. **20**, 105 (2014).

[48] Y. F. Ye, X. D. Liu, S. Wang, C. T. Liu, and Y. Yang, The general effect of atomic size misfit on glass formation in conventional and high-entropy alloys, Intermetallics **78**, 30 (2016).

[49] Q.-S. Zeng, Y. Ding, W. L. Mao, W. Luo, A. Blomqvist, R. Ahuja, W. Yang, J. Shu, S. V. Sinogeikin, and Y. Meng, Substitutional alloy of Ce and Al, Proc. Natl. Acad. Sci. USA. **106**, 2515 (2009).

[50] F. Spieckermann, D. Şopu, V. Soprunyuk, M. B. Kerber, J. Bednarčík, A. Schökel, A. Rezvan, S. Ketov, B. Sarac, and E. Schafler, Structure-dynamics relationships in cryogenically deformed bulk metallic glass, Nat. Commun. **13**, 1 (2022).

[51] R. E. Nettleton and M. S. Green, Expression in terms of molecular distribution functions for the entropy density in an infinite system, J. Chem. Phys. **29**, 1365 (1958).

[52] H. J. Raveché, Entropy and molecular correlation functions in open systems. I. Derivation, J. Chem. Phys. **55**, 2242 (1971).

[53] H. W. Sheng, W. K. Luo, F. M. Alamgir, J. M. Bai, and E. Ma, Atomic packing and short-to-medium-range order in metallic glasses, Nature (London) **439**, 419 (2006).

[54] D. A. Young, H. Cynn, P. Söderlind, and A. Landa, Zero-kelvin compression isotherms of the elements $1 \leqslant Z \leqslant 92$ to 100 GPa, J. Phys. Chem. Ref. Data **45**, 043101 (2016).